

Application of cell models to the melting and sublimation lines of the Lennard-Jones and related potential systems

D. M. Heyes^{1,*}, S. Pieprzyk^{2,†} and A. C. Brańka^{2,‡}

¹*Department of Physics, Royal Holloway, University of London, Egham, Surrey TW20 0EX, United Kingdom*

²*Institute of Molecular Physics, Polish Academy of Sciences, M. Smoluchowskiego 17, 60-179 Poznań, Poland*



(Received 30 May 2021; accepted 27 September 2021; published 19 October 2021)

Harmonic cell models (HCMs) are shown to predict the melting line of the Lennard-Jones (LJ) but not the sublimation line. In addition, even for the melting line, the HCMs are found to be physically unrealistic for inverse power potential systems near the hard-sphere limit, and for the Weeks-Chandler-Andersen system at extremely low temperatures. Despite this, the HCM accurately predicts the LJ mean-square displacement (MSD) from molecular-dynamics (MD) simulations along both lines after simple scaling corrections, to include the effects of anharmonicity and correlated dynamics of the atoms, are applied. Single caged atom molecular dynamics and Monte Carlo simulations provide further quantitative characterization of these additional effects, which go beyond harmonicity. The melting indicator and a modification of the cell model in a similar form are shown to be approximately constant along the melting line, which indicates an isomorph. The less well studied LJ sublimation line is shown not to be an isomorph, yet it still can be represented analytically very accurately by the relationship $k_B T = a\rho^4 + b\rho^2$, where a and b are constants (k_B is Boltzmann's constant, T is the temperature, and ρ is the number density). This relationship has been found previously for the melting line, but the two constants have opposite signs for the sublimation and melting lines. This simple formula is also predicted using a nonharmonic static lattice expression for the pressure. The probability distribution function of the melting factor indicates departures from harmonic or Gaussian behavior in the lower wing. Nevertheless, the mean melting factor is shown to follow a simple MSD Debye-Waller factor dependence along both the melting and sublimation lines. This work combining HCM and MD simulations provides a comparison of the melting and sublimation lines of the LJ system, which could provide the foundations for a more unified statistical mechanical description of these two solid boundary lines.

DOI: [10.1103/PhysRevE.104.044119](https://doi.org/10.1103/PhysRevE.104.044119)

I. INTRODUCTION

It has proven difficult to predict the freezing and melting coexisting densities of small molecule systems by statistical mechanics [1]. For about 50 years, molecular simulation has been used to determine these lines (see, e.g., Refs. [2–4]) starting from the pioneering work of Alder and Wainwright, who showed by molecular-dynamics (MD) simulation that hard spheres undergo a fluid-solid transition [5]. In addition, there are a number of approximate empirical single-phase “freezing rules” that only require information about the fluid side of coexistence (see, e.g., Refs. [6–8]).

Cell models (CMs) provide an analytically tractable highly simplified representation of liquids and solids [9–11]. The cell theory assumes that each atom or molecule is located in a cage formed from its first coordination shell of atoms in a liquid or crystalline arrangement. Each atom in the system is statistically equivalent, so only the mean-field properties of a single representative particle need be considered to represent the whole macroscopic sample, albeit at a significantly

approximate level. Cell models of liquids were applied to hard-sphere and inverse power (IP) potential systems in the 1960s and 1970s [12,13], and they are now finding increasing applications in the field of complex liquids [14], including proteins [15] and soft matter [16]. They are a computationally efficient way to map out approximately the phase diagram of a model system in which there are many adjustable parameters.

In recent years, accurate data for the melting lines of Lennard-Jones (LJ) [17,18] and related potential systems have become available. The predictions from a CM of the melting line (ML) can be compared with these data for validation purposes. Also, the CM results can be framed in the context of more recent theoretical advances, such as isomorph scaling [19], and hard-sphere based low-temperature limiting expressions [20,21]. In this work, the term “cell model” will refer to the situation in which the atoms are placed on a regular lattice and are either static or deemed to execute simple harmonic motion about the lattice sites, which is characterized principally in terms of the mean-square displacement (MSD) of each atom from its average position. MD simulations give essentially the exact MSD as they automatically take into account the anharmonicity of the potential energy surface experienced by the atoms and correlated atom motion. Apart from a few notable exceptions (see, for example, Refs. [22–24]), the CM usually neglects the consequences of anharmonicity and correlated atom motion on the MSD,

* Author to whom all correspondence should be addressed: david.heyas@rhul.ac.uk

† pieprzyk@ifmpan.poznan.pl

‡ branka@ifmpan.poznan.pl

although, as was shown in Ref. [23] and also in this study, their effects can be reproduced by scaling the harmonic CM MSD values in a systematic way.

It is shown here that for the Lennard-Jones potential system, the MSD can be represented accurately using a simple scaling correction to a static lattice CM formula for the MSD, and even better from the finite-temperature force constant determined as an average during an MD simulation. We find that there are some potentials and state point limits where the (harmonic) CM is not a physically reasonable model for the melting line, however. It is shown that the CM is physically unrealistic for steeply repulsive inverse power potential systems, and for the Weeks-Chandler-Andersen (WCA) system [25], at extremely low temperatures, where it behaves like a hard sphere.

The statistical properties of the displacement of the atom from its lattice site are explored using its probability distribution function (PDF), which can be represented well by a Gaussian for not too large values of the displacement. It is shown that the so-called melting factor (MF) or structure factor at a specific wave vector can be represented well by the Debye-Waller factor in which the MSD is a normalization constant in the exponent. These trends suggest that the collective motion and anharmonicity effects along the ML can be taken into account, at least at a mean-field level for certain properties, through the introduction of a multiplicative scaling constant.

The sublimation line (SL), which is the boundary on the solid side of solid-vapor coexistence (below the triple point temperature), has been less well studied by theory and molecular simulation. Its temperature density dependence has the opposite slope to that of the melting line. The performance of the CM approach for the SL line is assessed here also. For the Lennard-Jones case, a simple semiempirical formula, which only requires a single adjustable parameter, is derived based on a static lattice formula for the pressure. This semiempirical formula reproduces well the simulation-derived SL (i.e., the density-temperature relationship) for the Lennard-Jones case. It is also found that the MSD along the sublimation line obtained by MD can be represented well by a simple scaling of the regular lattice CM result.

Section II presents the cell models for melting and compares their performance with simulation data, Sec. III is concerned with the sublimation line, and conclusions are made in Sec. IV.

II. THE MELTING LINE

This work mainly considers the phase diagram of systems interacting with a pair potential, $\phi(r)$, of the Mie analytic form [26,27]

$$\begin{aligned} \phi(r) &= \phi_r(r) - \phi_a(r), \\ \phi_r(r) &= Q\epsilon \left[\frac{\sigma}{r} \right]^n, \\ \phi_a(r) &= Q\epsilon \left[\frac{\sigma}{r} \right]^m, \\ Q &= \frac{n}{n-m} \left(\frac{n}{m} \right)^{[m/(n-m)]}, \end{aligned} \quad (1)$$

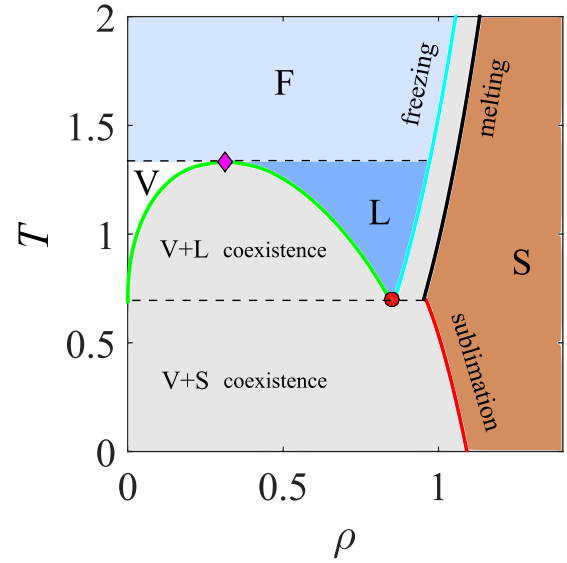


FIG. 1. Lennard-Jones phase diagram. The temperature is in LJ reduced units, i.e., T in real units is replaced by $k_B T/\epsilon$, where ϵ is the value of energy for a given molecule. The density is $\rho = N\sigma^3/V$ for N molecules in volume V . Key: F, supercritical fluid; S, solid; L, liquid; V, vapor. The solid colored diamond and circle represent the critical and triple point, respectively.

where r is the center-to-center distance between the two atoms, and ϵ and σ are the characteristic intermolecular interaction energy and molecular diameter, respectively, and where $n > m$ for thermodynamic stability [28]. The Lennard-Jones (LJ) potential is a special case of Eq. (1) in which $Q = 4$, $n = 12$, and $m = 6$. The quantities reported here are in the usual reduced units of ϵ and σ . The melting line of the WCA potential [25],

$$\phi_{\text{WCA}}(r) = \begin{cases} 4\epsilon \left[\left(\frac{\sigma}{r} \right)^{12} - \left(\frac{\sigma}{r} \right)^6 \right] + \epsilon, & r \leq 2^{1/6}\sigma, \\ 0, & r > 2^{1/6}\sigma, \end{cases} \quad (2)$$

is also considered. The well-characterized melting line of the IP potential [29],

$$\phi(r) = \epsilon \left(\frac{\sigma}{r} \right)^n, \quad (3)$$

is also readily treated by the cell theory. Although both are purely repulsive, a distinguishing feature of the WCA compared to the IP potential is that all its derivatives are zero for $r > 2^{1/6}$, which has consequences for its low-temperature melting line.

Figure 1 shows the Lennard-Jones potential phase diagram represented on the ρ - T plane. The ML and SL are separated by the triple point density and temperature whose values for the liquid and face-centered-cubic solid densities are 0.845 and 0.961, respectively, and 0.695 for the temperature [17]. The LJ melting line has been determined a number of times by MD and Monte Carlo (MC) (e.g., in Refs. [29–34]) and more recently by Schultz and Kofke [17,18].

A. Melting line theory

Apart from close to the triple point [4,19,35,36], the LJ melting (s) and freezing (f) lines are represented well

by [37–40]

$$\begin{aligned} k_B T_f(\rho) &= A_f \rho^4 - B_f \rho^2, \\ k_B T_s(\rho) &= A_s \rho^4 - B_s \rho^2, \end{aligned} \quad (4)$$

where k_B is Boltzmann's constant, and A_f and B_f apply to freezing. The constants A_s and B_s represent the melting line data. The two terms in Eq. (4) are the scaling expected from the inverse power $n = 12$ and 6 of the Mie potential, respectively. The additivity of the repulsive and attractive terms in a pair potential on the thermodynamic properties is the basis of perturbation theories of liquids, and in the formulations by Rosenfeld in a series of pioneering publications [41–44].

Approximate expressions for the melting line constants in Eq. (4) are given by Lindemann's cell model of melting, referred to here as the Lindemann melting rule (LMR) [6,45–47]. Only interactions with the first coordination shell are taken into account in the LMR. The LMR assumes the atoms are arranged on a perfect or regular lattice, and that the crystal melts when the root-mean-square amplitude of thermal vibration of an atom increases with temperature to a certain fraction of the nearest-neighbor distance, r_1 . The melting temperature follows by assuming that an atom independently vibrates harmonically about its average position. Despite its simplicity, the LMR has proved reasonably successful in various fields [6,45–47], notably in establishing relative values of the melting temperature for a range of solids in the same chemical class. The Lindemann parameter used in the theory is $\delta = \langle \Delta \mathbf{r}^2 \rangle^{1/2} / r_1$, where $\langle \Delta \mathbf{r}^2 \rangle$ is the MSD of the atom about its average position in the lattice (the time average is indicated by the angular brackets). The parameter δ used in predicting T_s should not be much greater than about 0.1 for the LMR model to be physically realistic.

The LMR cell model is a limiting case of a more general harmonic model in which (in effect) all the interacting atoms in the lattice are taken into account as forming the cage. The LMR analysis described below builds on that reported in Ref. [48] for bounded potential systems.

It is useful to consider first some basic thermodynamic properties of this perfect lattice approximation (e.g., for the pressure, which is used in the formula for the sublimation line in Sec. III).

1. Potential energy and pressure

Consider a perfect or regular lattice where the nearest-neighbor distance from a given atom is r_1 , the next-nearest-neighbor distance is r_2 , and so on. The numbers of atoms at shells defined through r_1, r_2, \dots are denoted by N_1, N_2, \dots . The lattice vector from the central atom is expressed as $\mathbf{r} = r_1 \mathbf{R}$, where \mathbf{R} is a dimensionless vector. If U is the potential energy of a cubic microcrystal of the lattice containing N atoms, then in the $N \rightarrow \infty$ limit,

$$\begin{aligned} u &= U/N = \frac{1}{2} \sum' \phi_r(r) - \frac{1}{2} \sum' \phi_a(r) \\ &= \frac{1}{2r_1^n} \sum' \frac{Q}{R^n} - \frac{1}{2r_1^m} \sum' \frac{Q}{R^m} \end{aligned}$$

$$\begin{aligned} &= \frac{A_n}{r_1^n} - \frac{A_m}{r_1^m}, \\ A_k &= \frac{Q}{2} \left(N_1 + \frac{N_2}{R_2^k} + \frac{N_3}{R_3^k} + \dots \right), \end{aligned} \quad (5)$$

where the factor of $1/2$ is added to avoid double counting in the potential energy per atom of the lattice. The summation in Eq. (5) is over the lattice vectors, and the prime denotes the omission of the central atom interacting with itself, which would contribute an infinite positive energy for $n > m$ Mie potentials. The summation is continued until the desired precision is obtained. The last line of Eq. (5) displays the first three terms of the lattice constant on the distance from the central atom. For a face-centered-cubic (fcc) lattice, $r_1 = c/\rho^{1/3}$, where $c = 2^{1/6}$, and R_1, R_2 , and R_3 are $1, \sqrt{2}$, and $\sqrt{3}$, respectively. The numbers in the first three coordination shells, N_1, N_2 , and N_3 , are $12, 6$, and 24 , respectively. For the bcc lattice, $c = 3^{1/2}/4^{1/3}$, R_1, R_2 , and R_3 are $1, 2/\sqrt{3}$, and $2\sqrt{2}/\sqrt{3}$, and N_1, N_2 , and N_3 are $8, 6$, and 12 , respectively.

The corresponding expression for the pressure, P , is similar to that of the potential in Eq. (5) as the virial term (the interaction part of P), $-\rho r \phi'(r)/3$, has the same powers of r_i as the potential energy and only differs from u in the prefactors. The pressure has a kinetic $P_k = \rho k_B T$ component and an interaction, P_c , part, which can be calculated using the lattice constants used for u defined in Eq. (5),

$$\frac{P_c}{\rho} = \frac{n A_n}{3 r_1^n} - \frac{m A_m}{3 r_1^m}. \quad (6)$$

Equations (5) and (6) can be written in the density-dependent form, which bears some similarity to Eq. (4),

$$\begin{aligned} u &= A_{\rho,n} \rho^{n/3} - A_{\rho,m} \rho^{m/3}, \\ \frac{P_c}{\rho} &= \frac{n}{3} A_{\rho,n} \rho^{n/3} - \frac{m}{3} A_{\rho,m} \rho^{m/3}, \end{aligned} \quad (7)$$

where $A_{\rho,k} = A_k/c^k$. Accurate values for $A_{\rho,12}$ and $A_{\rho,6}$ for the LJ potential were calculated in Ref. [49]. Table I contains a list of the $A_{\rho,k}$ for a range of k within the Mie framework [note the variable Q value in each case depends on n and m , as specified in Eq. (1)]. This static lattice approach can be extended to include the effects of atom vibration within a harmonic approximation, which is described next.

2. Harmonic lattice

The force constant K associated with the potential energy surface experienced by an atom is [23]

$$\begin{aligned} K &\equiv M \Omega_E^2 = \frac{1}{3} \nabla^2 \Phi \\ &= \frac{1}{3} \sum' \sum_{\alpha} \left(\frac{\phi'(r)}{r} \left[1 - \frac{\alpha^2}{r^2} \right] + \frac{\alpha^2}{r^2} \phi''(r) \right) \\ &= \frac{1}{3} \sum' \left(\frac{2}{r} \phi'(r) + \phi''(r) \right) \\ &= \frac{1}{3} \left(\frac{B_n}{r_1^{(n+2)}} - \frac{B_m}{r_1^{(m+2)}} \right), \end{aligned}$$

TABLE I. The lattice summation constants for the fcc lattice of the Mie $n : m$ potential for various values of n and m . The parameters A_n and A_m are defined in Eq. (5). Equation (7) specifies $A_{\rho,n}$ and $A_{\rho,m}$, and B_n and B_m are given in Eq. (8).

n	m	A_n	A_m	$A_{\rho,n}$	$A_{\rho,m}$	B_n	B_m	Q
288	6	6.65374	8.01734	2.36388×10^{-14}	4.00867	1.09994×10^6	425.911	1.10896
144	6	7.18859	8.66181	4.2847×10^{-7}	4.33090	296055	460.147	1.19810
72	6	8.20441	9.88580	2.00303×10^{-3}	4.94290	83881.9	525.170	1.36740
36	6	10.3030	12.4145	0.160984	6.20723	25963.5	659.502	1.71716
24	6	12.7008	15.3018	0.793800	7.65088	14020.8	812.886	2.11653
18	6	15.6053	18.7831	1.95067	9.39156	9545.13	997.829	2.59808
12	6	24.2638	28.9185	6.06594	14.4593	6367.15	1536.26	4.00000
11	6	27.7763	32.9176	7.79447	16.4588	6054.10	1748.71	4.55315
10	6	33.1120	38.8892	10.4296	19.4446	5873.32	2065.94	5.37914
9	6	42.1625	48.8000	14.9067	24.4000	5929.65	2592.44	6.75000
8	6	60.6917	68.5476	24.0855	34.2738	6536.82	3641.50	9.48148
7	6	117.915	127.613	52.5253	63.8065	9261.48	6779.27	17.6514
36	18	24.0000	24.0260	0.375001	3.00325	60480.1	14695.7	4.00000
24	12	24.0030	24.2638	1.50019	6.06594	26497.7	6367.15	4.00000

$$\begin{aligned}
 B_k &= Qk(k-1) \sum' \frac{1}{R^{(k+2)}} \\
 &= Qk(k-1) \left(N_1 + \frac{N_2}{R_2^{(k+2)}} + \frac{N_3}{R_3^{(k+2)}} + \dots \right), \quad (8)
 \end{aligned}$$

where M is the mass of the atom, Ω_E is the Einstein frequency [50], $\phi' \equiv d\phi(r)/dr$, and $\phi'' \equiv d^2\phi(r)/dr^2$. The second summation is over the three Cartesian coordinates, α , of the atoms.

For harmonic motion, and using Eq. (8),

$$\begin{aligned}
 k_B T &= \frac{1}{3} \langle \Delta \mathbf{r}^2 \rangle K = \frac{1}{3} \delta^2 r_1^2 K, \\
 \delta &= \frac{\sqrt{\langle \Delta \mathbf{r}^2 \rangle}}{r_1}, \\
 k_B T &= \frac{1}{9} \delta^2 \left(\frac{B_n}{r_1^n} - \frac{B_m}{r_1^m} \right) \\
 &= \frac{1}{9} \delta^2 \left(\frac{B_n}{c^n} \rho^{n/3} - \frac{B_m}{c^m} \rho^{m/3} \right), \quad (9)
 \end{aligned}$$

where a value of δ can be chosen to signify melting (i.e., $T = T_s$). The LMR expression is the first (nearest neighbor) or “ N_1 ” term in the expansion of B_k , and the converged value is referred to here as the harmonic lattice rule (HLR) approximation, which is the default model employed in this study unless stated otherwise. The last line in Eq. (9) is of the same form as in Eq. (4). The constants A_s and B_s in Eq. (4) in the harmonic approximation are from Eq. (9),

$$A_s = \frac{1}{9} \delta^2 \left[\frac{B_n}{c^n} \right], \quad B_s = \frac{1}{9} \delta^2 \left[\frac{B_m}{c^m} \right]. \quad (10)$$

If δ is a constant along the melting line, the LMR/HLR models are consistent with isomorphic scaling [36].

The constants defined in Eqs. (5), (7), and (8) for the attractive part of the potential are slower to converge with the shell index than those for the repulsive part. For the LJ (12:6) potential, for example, A_{12} for the first shell (Lindemann approximation) is only $\sim 1\%$ smaller than the limiting value, whereas B_6 is 17% too low.

3. Force-constant definitions

Equation (8) applied to a regular or perfect lattice at any density (temperature) along the melting or sublimation lines is referred to as K_p (“ p ” for “perfect” lattice). The thermal average value of Eq. (8) computed during the simulation at a given density (temperature) is denoted by K_T , which takes into account the departures of the atoms from their regular lattice sites. The force constant, K_T , can be obtained from two formally equivalent formulas,

$$\begin{aligned}
 K_T &= \frac{1}{3} \left\langle \sum' \left(\frac{2}{r} \phi'(r) + \phi''(r) \right) \right\rangle_{T,\rho} \equiv K_{T,1}, \\
 K_T &= \frac{\langle \mathbf{F}^2 \rangle_{T,\rho}}{3k_B T} \equiv K_{T,2}, \quad (11)
 \end{aligned}$$

where again the angular brackets denote a time average. The second definition in the last line of Eq. (11) is what is obtained for a harmonic oscillator, and also from the more generally applicable definition of the configurational temperature, T_{conf} [see, e.g., Eq. (21) in Ref. [51]]. It was confirmed numerically by MD simulations along the melting and sublimation lines that the two definitions of K_T [i.e., $K_{T,1}$ and $K_{T,2}$ in Eq. (11)] were statistically the same. The mean-square displacement computed directly from the MD simulations provides another route to an effective force constant, which is denoted by “ K_D ”,

$$\begin{aligned}
 K_D &= \frac{3k_B T}{\langle (\Delta \mathbf{r}_{\text{MD}})^2 \rangle}, \\
 \delta_D^2 &= \frac{3}{r_1^2} \frac{k_B T}{K_D}. \quad (12)
 \end{aligned}$$

The K_T and K_p will be different as K_p does not include cooperative motion and anharmonic effects which are present in the MD-modeled system. The difference between K_T and K_D has its origin in the fact that although K_T includes the effects of anharmonicity and cooperative motion through the distribution of configurations generated in the simulation, the HLR harmonic approximation formula is applied. Using these definitions of the force constants,

the corresponding δ^2 are

$$\delta_p^2 = \frac{3 k_B T}{r_1^2 K_p}, \quad \delta_T^2 = \frac{3 k_B T}{r_1^2 K_T}. \quad (13)$$

B. MD results along the melting line

Molecular-dynamics simulations were carried out of the solid phase along the LJ melting and sublimation lines. The state points were obtained from the analytic expressions given by Schultz and Kofke [17,18]. Simulations were also carried out along the $P = 0$ isobar approximation for the sublimation line discussed in Sec. III. These calculations were conducted by starting from a perfect lattice at the density given by the formula in Refs. [17,18] for each temperature. An equilibration stage of $\sim 50\,000$ time steps was conducted in which the density was gradually adjusted each time step by a highly damped feedback formula, of the form $\rho - \kappa(\langle P \rangle - P_{\text{targ}}) \rightarrow \rho$, where ρ is the instantaneous density, $\langle P \rangle$ is the average pressure up to the current time step, P_{targ} is the target pressure (here = 0), and $\kappa = 0.0001$. The average of this feedbacked density was taken for the production simulation run.

The MD time step was $\Delta t = 0.004/\sqrt{T}$, and for the LJ potential the interaction truncation distance r_c was half the simulation box sidelength (see Ref. [55]). The number of particles in the simulation cell, N , was typically 500, 864, and 1372 to assess the N -dependence. The production phase computations at each state point on the solid side of the melting and sublimation line curves were conducted for typically $1 - 2 \times 10^5$ time steps. Thermostatting was conducted using NVT dynamics with the Nosé-Hoover (NH) thermostat [56,57], employing a time constant of three LJ time units and also by velocity rescaling [55], which were found to give statistically indistinguishable results. All the codes used were written in-house in FORTRAN.

Figure 2(a) compares the melting temperature of the LJ system from simulation in Refs. [17,18] with the HLR prediction formula given in Eq. (9). On the scale of the figure, the value of $\delta = 0.105$ predicts quite well the actual melting line obtained by simulation for the whole temperature range considered, apart from close to the triple point. Data for the same quantities for the IP $n = 12$ system melting line are also shown (where density has been converted to the $Q = 4$ LJ units). There is a vertical difference between the IP and LJ data, which only slowly decreases with increasing density.

The sensitivity of the degree of agreement to the value of δ is shown in the Supplemental Material [58]. Figure 2(b) shows the density dependence of the constants, A_s and B_s , defined in Eq. (4) fitted to the ML $\rho(T)$ parametrized formula presented in Ref. [18]. For temperatures 0.694, 1.00, 1.50, and 2.0, the values of A_s are 3.165, 2.327, 2.083, and 2.009, respectively. The corresponding B_s are 2.169, 1.371, 1.111, and 1.0215. The high-temperature limiting values of A_s and B_s are 1.8985 and 0.8126, respectively, whose data points are given in Fig. 2(a), which shows that the simulation derived curve only noticeably departs from this formula in the figure for densities below about 1.1. The HLR values of A_s and B_s according to Eq. (10) with $\delta = 0.105$ (1.950 and 0.941) are shown in the figure, and so are the IP values from Ref. [35] (1.872 and 0.7248). For densities in excess of about $\rho = 3.0$

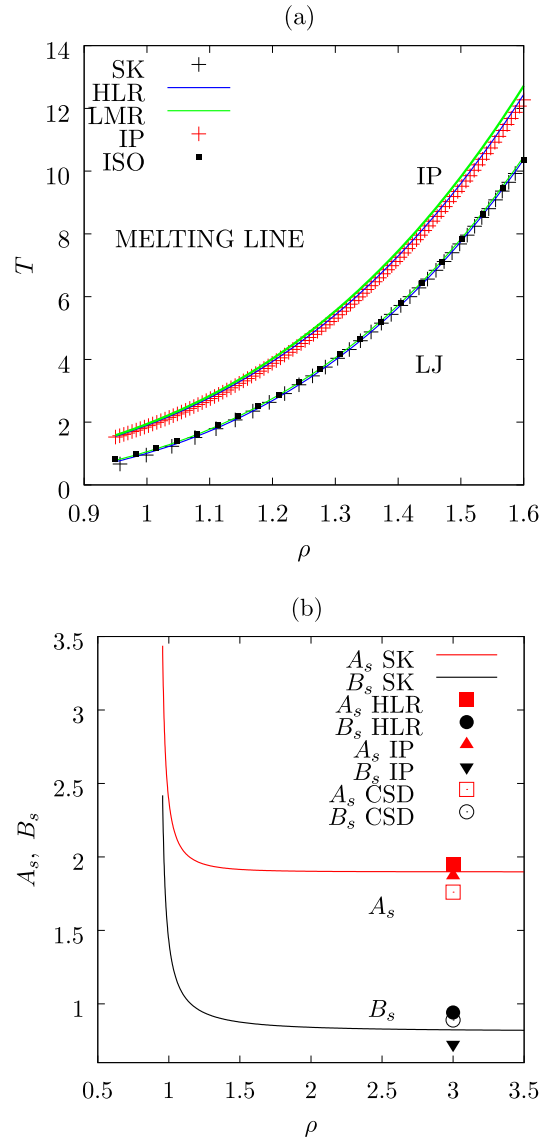


FIG. 2. (a) The melting temperature of the LJ system from simulation (“SK”) in Refs. [17,18] compared with the prediction of HLR from Eq. (9) using $\delta = 0.105$ is shown. The melting line isomorph (“ISO”) of the analytic form, $k_B T = 1.8985\rho^4 - 0.8126\rho^2$, is shown. (b) The density dependence of the constants, A_s and B_s , defined in Eq. (4) is shown using the ρ, T parametrized formula given in Table I, line 2 in Ref. [18] (SK, continuous line). The symbols are HLR from Eq. (10) with $\delta = 0.105$; “IP” are the separate values from Ref. [35]. The LJ melting line invariants from Ref. [54] are denoted by “CSD”. These symbols are arbitrarily placed at $\rho = 3$.

(or $T > 147$), the B_s value is within about 1% of the high density (temperature) limiting value, and 0.0003% for A_s (which converges more rapidly). With increasing density, the values of A_s and B_s approach the limiting (“isomorph”) values. From a practical point of view, one might reasonably take the transition from nonisomorph to isomorph state density to be in the density range of 2–3. The deviation from the melting line from an isomorph was accounted for quantitatively by the theory developed in Ref. [36], which predicted the variation of, for example, the Lindemann ratio along the melting line

with no free parameters (once a simulation at $T = 2$ has been carried out).

The contribution from the B_s term becomes in relative terms smaller than the A_s term with increasing density because of the additional ρ^2 and ρ^4 factors in Eq. (4). The contribution of B_s at all physically reasonable densities and temperatures cannot be ignored, however, and it is responsible for the offset between the IP and LJ curves in Fig. 2(a).

The solid-fluid coexistence melting lines of the $n : 6$ Mie potential system where $7 \leq n \leq 12$ obtained by MD and MC techniques are reported in Refs. [31,59], respectively. Using this simulation data in Eq. (9), the HLR value for δ by examples of the $7 : 6$, $8 : 6$ are similar in shape but slightly lower than that of $12 : 6$, as shown in the Supplemental Material [58].

For any $n > 3$, each IP curve on the ρ - T plane, including the melting line, is an exact isomorph, and, for this reason, the Lindemann criterion is rigorously obeyed, i.e., δ must be a constant. This can be proved by writing r_1 and K in isomorph units (written for property X by “ \tilde{X} ”), i.e., $r_1 = \tilde{r}_1 \rho^{-1/3}$ and $K = \tilde{K} k_B T \rho^{2/3}$ in the first line of Eq. (9). The fact that the value of the mean-square displacement at melting may depend on the IP exponent does not formally invalidate the Lindemann criterion for that system. Whether the value of δ is physically realistic is another matter, which is considered immediately below.

Equation (9) applied to the IP potential system gives a formula for δ_{IP} (which makes use of the known melting density and temperature [29]),

$$\delta_{IP} = \left(\frac{9k_B T_s c^n}{B_n \rho_s^{n/3}} \right)^{1/2}. \quad (14)$$

In the large n limit, B_n can be replaced with insignificant error by its LMR approximation, i.e., $B_n = 12n(n-1)$ (note here $Q = 1$), which when substituted in Eq. (14) gives

$$\lim_{n \rightarrow \infty} \delta_{IP} = \left(\frac{3}{4} \frac{c^n}{n(n-1)} \left[\frac{k_B T_s}{\rho_s^{n/3}} \right] \right)^{1/2} \quad (15)$$

for the fcc lattice. Then in the hard-sphere limit (i.e., $n \rightarrow \infty$), $\rho \rightarrow 1.0376$ for $T_s = 1$ (exploiting the exact relationship that $\rho_s^{n/3}/T_s = \text{const}$), and the dominant term in Eq. (15) for large n is c^n , which is $2^{n/6}$ for the fcc lattice. The value of δ_{IP} in Eq. (15) diverges in the $n \rightarrow \infty$ limit because the ratio $2^{1/6}/\rho_{HS}^{1/3} = 1.109 > 1$ for the fcc lattice. The data in Fig. 3 show that δ_{IP} increases dramatically for $\sim n > 40$ due to the dominance of the c^n term in Eq. (15). This indicates that δ_{IP} used in the LMR and HLR treatments diverges in the hard-sphere limit, which is unphysical as then $\delta \gg 1$.

Figure 4 presents data for the melting line of the WCA fluid from several sources. The LMR prediction with $\delta = 0.105$ is reasonable at liquidlike densities but overestimates the melting temperature for extremely low temperatures. Stillinger [21,49] showed that particles interacting with a repulsive Gaussian pair potential behave increasingly like hard spheres in the low-temperature limit (i.e., $T \ll 1$ in reduced units). The low-temperature part of the melting line can be reproduced increasingly accurately by equating the Boltzmann factor, B_f , to a number $\sim 1/2$. The same procedure

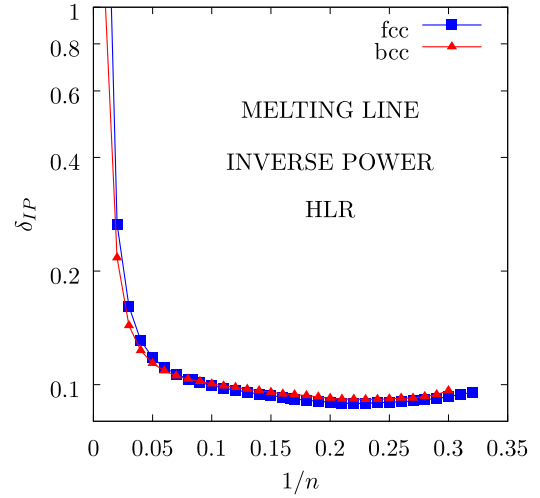


FIG. 3. The root-mean-square displacement parameter, δ_{IP} , defined in Eq. (15) with HLR. Key: Ref. [29], “fcc-fcc” is the δ_{IP} predicted from the fcc lattice formula using the calculated ρ_{fcc} , and “bcc-bcc” is the δ_{IP} predicted for the bcc lattice using the calculated ρ_{bcc} .

applied to the WCA potential gives

$$B_f = e^{-\beta \phi_{WCA}(r)} = 1/2,$$

$$r^{-3} = \left(\frac{[1 + \sqrt{T \ln 2}]}{2} \right)^{1/2} = (\sigma/\sigma_{HS})^3,$$

$$\rho_{HS} = \frac{N}{V} \sigma_{HS}^3,$$

$$\frac{N}{V} \sigma^3 = \frac{N}{V} \sigma_{HS}^3 (\sigma/\sigma_{HS})^3,$$

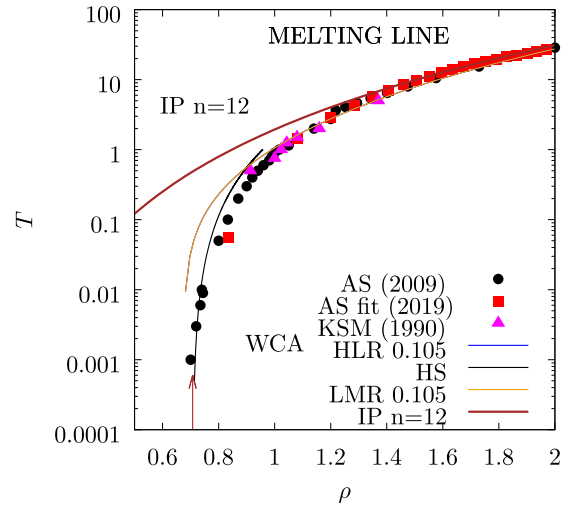


FIG. 4. The melting temperature of the WCA [i.e., see Eq. (2) and Ref. [25]] system compared with the prediction of HLR from Eq. (9). The simulation melting temperature-density data from Refs. [60,61] (AS) and Ref. [62] (KSM) are shown as symbols. The black line (HS) is the prediction of Eq. (16) using the hard-sphere melting density. The curve IP is for IP $\delta = 0.105$. The brown vertical arrow indicates the limiting value of $\rho_{WCA} = 1/\sqrt{2}$ in the $T \rightarrow 0$ limit.

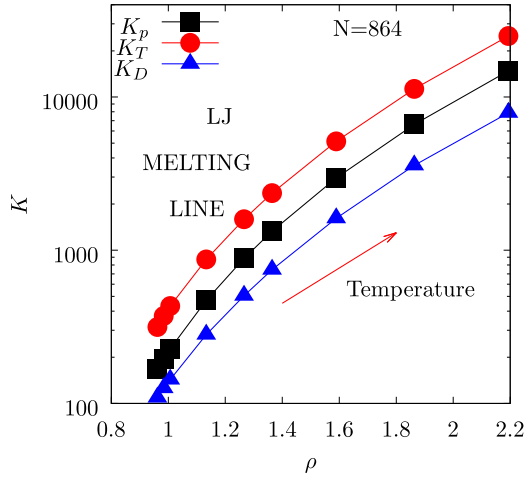


FIG. 5. The density dependence of the force constants along the LJ melting line. K_p is evaluated from Eq. (8) applied to a perfect lattice at the given density. K_T is defined in Eq. (11), and K_D is in Eq. (12). The T values are from left to right: 0.7, 0.85, 1.0, 2.0, 3.5, 5.0, 10, 20, and 40.

$$\rho_{\text{WCA}} = \rho_{\text{HS}} \left(\frac{[1 + \sqrt{T \ln 2}]}{2} \right)^{1/2}, \quad (16)$$

where $\beta = 1/k_B T$, $\rho_{\text{HS}} = 1.0376$ is the hard-sphere melting density [63], and ρ_{WCA} is the predicted number density in LJ units of the solid along the melting line. The pair separation distance r in Eq. (16) is that value of the center-to-center distance between the two atoms which satisfies the relationship in the first line of this equation. Because of the finite nonzero range of the WCA potential, $r \leq 2^{1/6}$, it follows from Eq. (16) that $\rho_{\text{WCA}} \geq 1/\sqrt{2}$ in the low-temperature limit, which is confirmed in Fig. 4 by comparison with literature simulation ML data.

Figure 5 shows that K_p , K_T , and K_D , as defined in Eqs. (8), (11), and (12), respectively, increase with density along the melting line. The order of magnitude is $K_T > K_p > K_D$ at each density (temperature). The reason for this is that K_p just gives the perfect lattice harmonic value, but with increasing temperature the anharmonic term (the fourth-order derivative of the effective potential experienced by the atoms) becomes increasingly important. The anharmonic term acts as an extra source of “confinement” of the atom in its cage. There have been many publications quantifying anharmonic effects on the lattice dynamics of crystals [23,64–72]. This additional term in the effective potential increases the effective force constant to a greater extent as temperature increases, and therefore $K_T > K_p$. In addition to the effects of the anharmonic potential term on the dynamics, the cooperative motion between the atoms causes an additional “softening” of the confining cage, which has the biggest effect on K_D , and not K_T . The force constants K_T obtained from 500 and 864 particle system simulations are statistically indistinguishable. K_D , in contrast, does exhibit a small but noticeable systematic N -dependence, as would be expected for a quantity derived from a fluctuation property, which is here the average atom mean-square displacement.

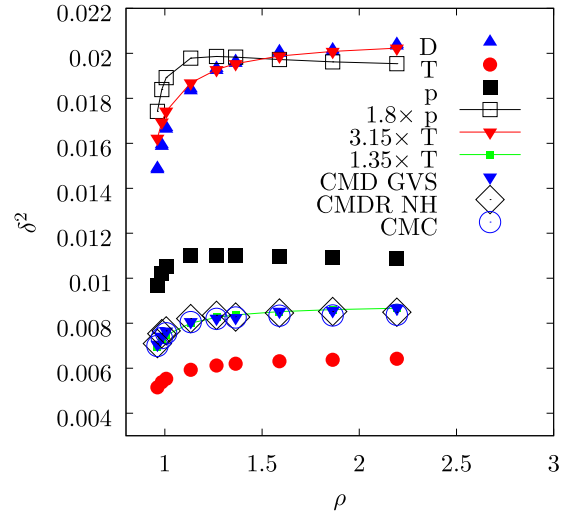


FIG. 6. As for Fig. 5 except that the corresponding scaled mean-square displacements or δ^2 are shown. D refers to MD using Eq. (12) for $N = 864$. The temperatures used from left to right were 0.7, 0.85, 1.0, 2.0, 3.5, 5.0, 10, 20, and 40. Equation (13) was employed to obtain δ_p^2 (“ p ”) and δ_T^2 (“ T ”). Data using the CMD, CMDR, and CMC methods are also shown.

Figure 6 presents the values of δ^2 along the melting curve as a function of density. The quantities δ_p^2 and δ_T^2 were calculated from K_p and K_T using Eq. (13), and δ_D^2 directly from the MD computations with Eq. (12). Figure 6 reveals that $\delta_D^2 > \delta_p^2 > \delta_T^2$ as expected from the order of the force constants in Fig. 5. The cell-based approaches founded on the simplest harmonic or Einstein model approximation yield δ or K , which differ considerably in magnitude from those calculated directly from MD. As discussed and shown by Holian [23], this is to be expected as the anharmonic and atom-atom correlation effects are absent in K_p . In fact, these additional factors are only partially included in K_T . Their contributions are not negligible at melting. The results in Fig. 6 suggest that the main differences between δ_p^2 and δ_T^2 from δ_D^2 may be corrected for by a simple constant multiplicative factor applied to all the data points. Debye took into account long-wavelength correlations between the atoms in a solid, which lead [23,73,74] to a correction factor to the (“Einstein”) force constant, K_p , or equivalently multiplication of δ_p^2 by 1.8. Figure 6 shows that the Debye modification gives remarkably good agreement with the MD δ^2 along the melting line, as was also commented on and proved by Holian in Ref. [23]. However, there are still qualitative discrepancies, in particular that $1.8 \times \delta_p^2$ decreases more sharply in the density region 1.0–1.4 than δ_D^2 . The shape of δ_D^2 is closer to that of δ_T^2 . Figure 6 also shows that $3.15 \times \delta_T^2$ follows well δ_D^2 , even better than the δ_p^2 scaling.

To explore further the effects of anharmonicity and cooperative motion, a variant of the MD simulation was used in which each atom was surrounded by a rigid fcc regular lattice at that density. The mobile atom interacted with the rigid atoms through the LJ potential. This procedure eliminated any cooperative motion, as each atom was only allowed to explore its own ideal rigid crystal cage. This modification of

the usual procedure was a simulation realization of the cell model but which also included the anharmonic terms in the potential energy landscape. This cell MD modification is referred to as ‘‘CMD.’’ In addition, another variant, ‘‘CMDR,’’ in which the surrounding rigid lattice was formed from a frozen equilibrated configuration at the used density and temperature, was used. This has the effect of smearing out the cage wall atom locations to make the model more realistic. Each mobile atom experienced a different fixed randomized lattice arrangement. Also METROPOLIS Monte Carlo [57] versions of the cell simulation techniques were implemented, denoted by CMC and CMCR for the regular and randomized cage forms, respectively.

Figure 6 shows the CMD δ^2 values along the ML using a global velocity rescaling thermostat to control the temperature. The (global) velocity rescaling factor was determined from all mobile but independently moving atoms combined at each time step. The data for a CMDR simulation with a NH thermostat evolved separately for each mobile atom are also shown, as is a run carried out with CMC. They all give statistically the same δ^2 , which indicates that a single caged atom simulation can be reliably carried out. The cell simulations δ^2 are uniformly above δ_7^2 by a factor of ~ 1.35 , as indicated in the figure. The difference in shape between δ_p^2 and δ_7^2 at low densities can therefore be attributed to the inclusion of some anharmonicity in the latter. The cell simulation method includes additional anharmonic features not present in the two cell model regular lattice treatments. However, the entire anharmonic contribution is only obtained from the MD simulations, as K_D then includes the cooperative contribution to the displacements, which affects the potential energy surface experienced by the atoms, and this feature is absent in CMD and CMDR.

1. Atom displacement statistics

The MD simulations provide the opportunity to explore in more detail the nature and statistical distribution of the departures of the atoms from their mean lattice sites, $\Delta\mathbf{r}$. This is the vector of an atom from its mean position, i.e., it is the displacement vector. Figure 7 shows the radially averaged density distribution, $\rho(\Delta r)$ [75], for two temperatures along the solid side of the LJ melting line (further definition details are given in Appendix A). The data for systems consisting of $N = 500$ and 864 particles gave statistically indistinguishable profiles. The Gaussian approximation is very good, except after $\rho(\Delta r)$ has decayed by about 99%, where the decay is slower than Gaussian. This feature suggests that there were infrequent relatively large departures of the atoms from their average lattice sites, presumably caused by correlated motion between nearby atoms. However, this feature has little effect on the average value of the mean-square displacement. This can be seen from the integrated mean-square displacement

$$\langle[\Delta\mathbf{r}]^2(X)\rangle = 4\pi \int_0^X [\Delta r]^2 \rho(\Delta r) d\Delta r, \quad (17)$$

which is also shown in the figure. It may be seen in Fig. 7 that $\langle[\Delta\mathbf{r}]^2(X)\rangle$ has essentially reached a plateau before noticeable differences in $\rho(r)$ from the Gaussian form are evident. The accuracy of the Gaussian approximation involving δ_D^2 indi-

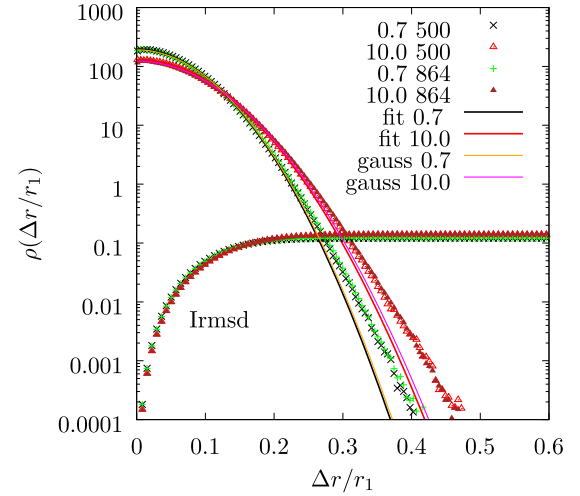


FIG. 7. The radial density function, $\rho(\Delta r)$, defined in Eq. (A2) for two state points along the LJ melting line, where $T = 0.7$ and 10, which are indicated in the figure. The number of atoms, N , is 500 and 864, which are also given in the figure. The lines ‘‘gauss’’ are the Gaussian PDFs defined in Eq. (A1) where the $\langle\delta^2\rangle$ are taken from the MD simulation. A least-squares fit to the Gaussian function in Eq. (A1) was made in each case, where α_G was treated as an adjustable parameter (the fit is for $\Delta r/r_1 \leq 0.3$) and denoted by ‘‘fit.’’ The integrated root-mean-square displacement (‘‘Irmsd’’) computed for $N = 864$ from Eq. (17) for the two temperatures is also shown in the figure.

rectly suggests that K_D and δ_D^2 could be used in mean-field analytic approximations of solid-state behavior.

The structure factor, $S(\mathbf{k})$, where \mathbf{k} is the reciprocal-lattice vector, forms the basis of the Hansen-Verlet freezing rule [76], and when expressed in isomorph units, $S(\mathbf{k}/\rho^{1/3})$ is constant along an isomorph [19]. The related melting factor MF is [57,77]

$$\text{MF} = \left[\frac{1}{N} \sum_{i=1}^N \cos(\mathbf{k} \cdot \mathbf{r}_i) \right]^2 + \left[\frac{1}{N} \sum_{i=1}^N \sin(\mathbf{k} \cdot \mathbf{r}_i) \right]^2, \quad (18)$$

and $0 \leq \text{MF} \leq 1$, which is routinely used in simulation as a practical tool to assess when an initial lattice has melted (ranging from 0 for a totally random arrangement of atoms to 1 for a perfect crystal). Its variation along the melting line was calculated according to Eq. (18), for the case of $k = 2\pi/\Delta L$, where ΔL is the interlayer spacing along the (1, 0, 0) direction of the fcc lattice. In the harmonic approximation, the melting factor is the Debye-Waller factor (DWF) [65] when there are no spatial and temporal correlations between the atoms, and

$$\text{DWF} = \exp(-a\delta^2), \quad (19)$$

where $a = (2\pi\sqrt{2})^2/3 = 26.32$ for this choice of wave vector.

The melting factor probability distribution functions (PDFs) at several temperatures along the LJ melting line are given in Fig. 8(a). The distribution is to a very good approximation Gaussian near the top of the PDF but is slightly skewed to lower values in the wings, an effect that increases with temperature. This indicates that (as was interpreted from Fig. 7) there are some configurations in which the departures

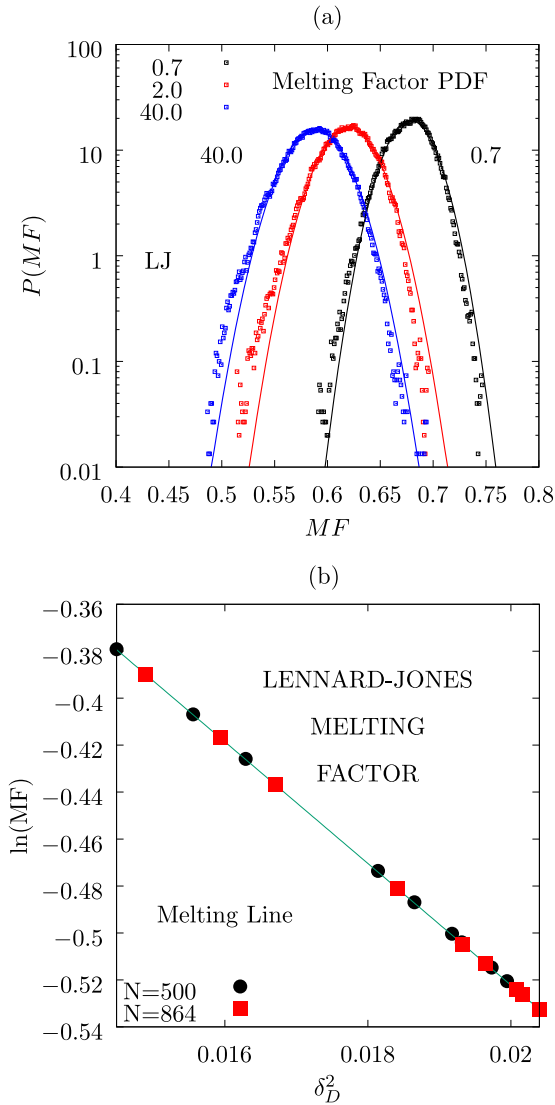


FIG. 8. (a) Melting factor PDF for the melting line at three temperatures, $T = 0.7, 2.0,$ and 40 . MD data for $N = 864$ are shown. (b) The mean melting factor against δ_D^2 , where a linear regression for $N = 864$ gives an intercept and slope of $-0.0040(3)$ and $-25.91(1)$, respectively. This demonstrates that the MD data adhere well to Eq. (19).

of the atom average positions are particularly large due to correlated motion. These give rise to a more disordered array at that instant than is expected from independent harmonic motion.

Figure 8(b) presents the mean melting factor as a function of δ_D^2 along the LJ melting line, plotted on a lin-log scale. The fact that δ_D^2 varies along the ML *at all* indicates that for temperatures close to the triple point value, the ML departs a little from an isomorph, at least according to the δ equal to a constant criterion [35,36,78]. Data points along this line are evidence of varying degrees of departure from isomorph behavior. The linearity of the data indicates that the MF is to a very good approximation equal to the Debye-Waller factor [65] using δ_D^2 as the required parameter. The least-squares fit slope is within $\sim 2\%$ of the formal value of a given in

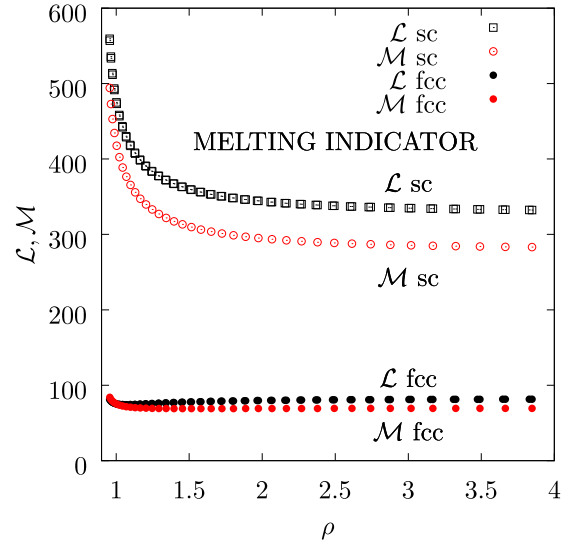


FIG. 9. The density dependence of \mathcal{L} calculated using Eq. (B1), and \mathcal{M} is defined in Eq. (B2) along the melting line of the LJ system. The parameters B'_{12} in Eq. (B2) are 1.016 364 and 1.004 916 for the sc and fcc crystals. The parameters B'_6 are 1.157 635 and 1.066 83 for the sc and fcc crystals.

Eq. (19) for the chosen interlayer direction. It was also found that the values of the even order cumulants of the particle displacements were several orders of magnitude smaller than the second cumulant (i.e., the MSD case). From a practical point of view, Fig. 8(b) indicates that the MF can be obtained from δ_D^2 using Eq. (19), or *vice versa*, which could be useful in developing analytic theories of the ML, which is not reliant on using a cell model.

A structure-independent freezing indicator, \mathcal{L} , has been proposed and applied to a wide range of model potential systems,

$$k_B T = \frac{1}{\mathcal{L}} (r^2 \phi''(r))_{r=\bar{r}}, \quad (20)$$

where $\bar{r} = 1/\rho^{-1/3}$ was used for the mean interparticle distance in those previous studies [37,38,46,52,53]. In Eq. (20), \mathcal{L} is an adjustable constant that takes on a roughly comparable role to δ^{-2} in the LMR and HLR treatments. Equation (20) has primarily been used for the freezing transition (i.e., $\rho = \rho_f$), but it has also been applied to melting [37], where the density along the melting line instead was used. The mean distance \bar{r} used for a fluid is also that of a simple-cubic lattice at the same density. For the crystal phase, the more general definition, $\bar{r} = c/\rho_s^{-1/3}$, can be used, which enables the behavior of different lattice types to be distinguished while retaining the simplicity of Eq. (20). This is the principal innovation here, where Eq. (20) can be used also as a melting indicator (MI). For a given crystal type, the parameter c and density define \bar{r} . For the simple cubic and fcc lattices, $c = 1$ and $2^{1/6}$, respectively, and $\bar{r} \equiv r_1$ is chosen. No other details of the lattice are required for \mathcal{L} . The expression for \mathcal{L} for the Mie potential is given in Appendix B, which also includes the definition of another related quantity, \mathcal{M} , which is a reexpression of the HLR formula in Eq. (9) in a similar format to that of \mathcal{L} .

Figure 9 shows that the simple-cubic lattice curve has a high density limiting $\mathcal{L} \simeq 350$, which is in good agreement with Ref. [37]. For the simple-cubic lattice, the formula, $\bar{r} = \rho^{-1/3}$, is in fact the same as that used in the previous work on freezing in Ref. [37]. The value of \mathcal{L} is seen to be highly sensitive to lattice type (through \bar{r}), however, and it reduces to ~ 100 for the fcc lattice, which is the correct crystal form along the ML. The corresponding fcc melting curve is much less density-dependent than that of the sc lattice, for ρ greater than about 1.5. The melting indicator in its current formulation is very close to the HLR model, and its density dependence is qualitatively similar to \mathcal{M} , which is also shown for both lattice types in Fig. 9. The \mathcal{M} values are slightly lower than the \mathcal{L} at a given density in both sc and fcc cases.

Figure 9 demonstrates that for the fcc solid, the melting indicator, \mathcal{L} , and the related parameter, \mathcal{M} , are nearly constant along the melting line for densities in excess of about 2.0. This trend follows from the fact that the melting line is an approximate isomorph as the isomorph description, $h(\rho)/k_B T = \text{const}$ [79], is satisfied. The combination of Eqs. (3) and (16) in Ref. [79] gives the definition of \mathcal{L} in Eq. (20) above.

To summarize, further evidence is presented of the effectiveness of a quasiharmonic treatment of atomic dynamics along the solid melting line. It is shown that both anharmonicity and the effects of collective dynamics can be incorporated into a harmonic cell model at a mean-field level (i.e., by a simple scaling factor) to reproduce the simulation mean-square displacements (see Fig. 6). In addition, the statistics of the atom displacements from their average locations are shown to be essentially (but not completely) Gaussian in form, in which the key constant involves the mean-square displacement of the atoms obtained directly by MD. The Debye-Waller factor is consequently expressed accurately in terms of just the MD MSD, and this is shown to be the same as the melting factor in this instance. The Lindemann cell model is not always a physically realistic representation of the melting line in regard to the magnitude of the mean-square displacements, however, as shown for steeply repulsive inverse power systems and for the WCA low-temperature limit. Nevertheless, despite these limitations, the harmonic cell models perform remarkably well in representing melting lines in general, and better than might have been expected because of their simple foundations.

In the next section, the methodology used for the melting line in this section is applied and adapted for the sublimation line.

III. SUBLIMATION LINE

Solids at temperatures below the triple point along the SL have been the subject of only a few simulation studies (e.g., Refs. [17,18,80,81]). It is essential for any system to have an attractive component to the pair interaction for it to have a SL, otherwise the melting line continues down to the $T \rightarrow 0$ limit, as is evident in Fig. 4 for the WCA potential and has to be the case for the IP potential whose ML consists of lines of constant $\rho^{n/3}/T$. Figure 1 shows that the temperature dependence of the sublimation curve is qualitatively different from that of the melting curve, in that the density *decreases*

as temperature increases. The SL of the LJ system has been determined with the aid of simulation in Refs. [17,18,80].

The pressure along the sublimation line is very small ($< 10^{-3}$ in LJ units [80]), which can be exploited to obtain an approximate expression for the temperature dependence of the density of the solid along the sublimation line, ρ_{sub} , by imposing the condition that $P = 0$. Starting from Eq. (7) and where $\alpha_T = 1$ in the equation below, the SL is predicted to be

$$\begin{aligned} P &= P_k + \alpha_T P_c, \\ 0 &= \rho_{\text{sub}} k_B T_{\text{sub}} + \alpha_T [4A_{\rho,12} \rho_{\text{sub}}^5 - 2A_{\rho,6} \rho_{\text{sub}}^3], \\ k_B T_{\text{sub}} &= -\alpha_T [4A_{\rho,12} \rho_{\text{sub}}^4 - 2A_{\rho,6} \rho_{\text{sub}}^2], \\ \rho_{\text{sub}} &= \left(\frac{A_{\rho,6} + \sqrt{A_{\rho,6}^2 - 4A_{\rho,12} k_B T_{\text{sub}} / \alpha_T}}{4A_{\rho,12}} \right)^{1/2}, \end{aligned} \quad (21)$$

where ρ_{sub} and T_{sub} are the density and temperature, respectively, along the SL. Figure 10(a) shows that the curve from Eq. (21) when $\alpha_T = 1$ has the correct (negative) slope but is significantly smaller than those of the simulation-derived curves [17,18]. This might be expected, in part, as the $\alpha_T = 1$ special case is based on a static lattice regular crystal formula without contributions from anharmonicity and cooperative motion of nearby atoms. An optimum value of α_T was obtained by fitting the sublimation line coexistence density and temperature to the formula of the form

$$k_B T_{\text{sub}} = B_{\text{sub}} \rho_{\text{sub}}^2 - A_{\text{sub}} \rho_{\text{sub}}^4, \quad (22)$$

which follows from Eq. (21). Then,

$$\begin{aligned} a_{12} &= A_{\text{sub}} / (4A_{\rho,12}), & a_6 &= B_{\text{sub}} / (2A_{\rho,6}), \\ \alpha_T &= (a_{12} + a_6) / 2, \end{aligned} \quad (23)$$

taking the values of $A_{\rho,12}$ and $A_{\rho,6}$ from Table I, which gives a value $\alpha_T = 0.11555$ (as a_{12} and a_6 are 0.11559 and 0.11551, respectively). The formula in the last line of Eq. (21) with this value of α_T reproduces the literature SL data very well at all temperatures, as is evident in Fig. 10(a) and Table II, despite its simplicity and only requiring a single fitted parameter. The parameters A_{sub} and B_{sub} are 2.80368 and 3.34030, respectively. Note that apart from a sign change, Eq. (22) has the same analytic form as the melting line formula of Eq. (4), yet it is not an isomorph. If the ML is considered to be dominated by the repulsive part of the potential (i.e., viewed from a perturbation theory perspective), then the reference state for the SL appears to be determined to some extent by the attractive part of the potential. The configurational part of the pressure along the SL is negative, so the crystal is under tension along this line.

If T_P is the temperature obtained directly by MD subject to the condition $P = 0$, and T_{sub} is obtained by the formula in Eq. (21) using $\alpha_T = 0.11555$, the difference, $\Delta T_1 = T_P - T_{\text{sub}}$, can be defined. If T_{SK} is the temperature obtained from the Schultz-Kofke formula [17,18], then another temperature difference, $\Delta T_2 = T_{\text{SK}} - T_{\text{sub}}$, is specified. Figure 10(a) shows the density dependence of ΔT_1 and ΔT_2 , which indicates that the sublimation temperature calculated from the semiempirical formula in Eq. (21) agrees better than 1% with the exact temperature values near the top of the coexistence line, but

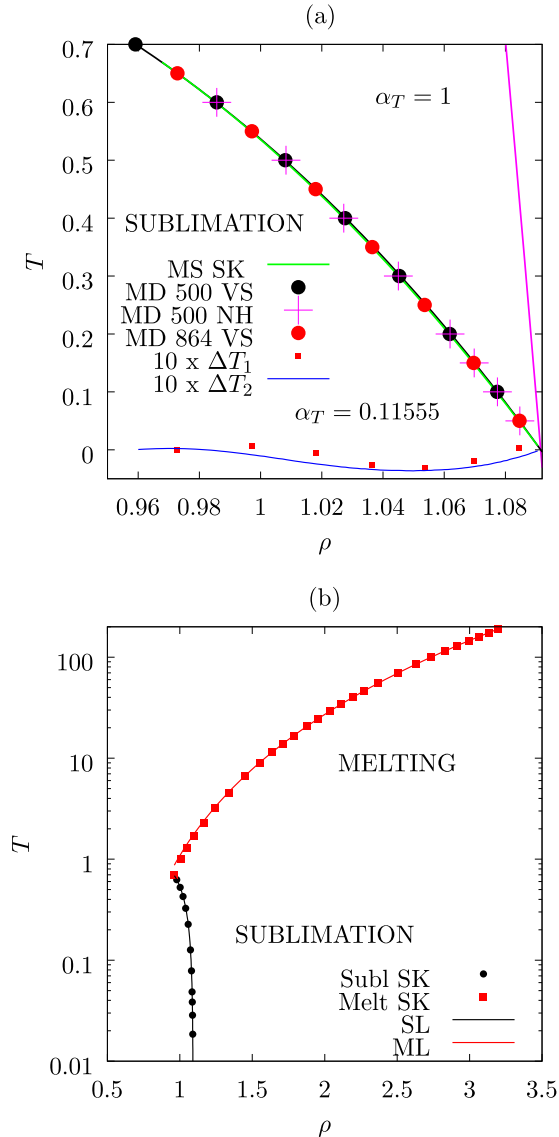


FIG. 10. (a) The sublimation curve derived from simulation data [17,18] (SK) is the green line, and MD refers to simulation taking $P = 0$. The solid magenta line is the formula in Eq. (21) with $\alpha_T = 1$, and the black solid line is the result of a least-squares fit derived correction, $\alpha_T = 0.11555$ in Eq. (21) (it is hardly distinguishable from the green line). MD data for $N = 500$ and 864 are shown. The quantities ΔT_1 and ΔT_2 are defined in the main text. Data for velocity scaling (VS) and the Nosé-Hoover (NH) thermostats are shown. (b) The SK melting and sublimation lines (shown as symbols) compared with the formulas in Eq. (4) where $A_s = 1.8985$ and $B_s = 0.8126$ (ML) for melting, and Eq. (22) where $A_{\text{sub}} = 2.80368$ and $B_{\text{sub}} = 3.34030$ (SL) for sublimation, given as continuous lines.

overestimates it by a few percent for $T < 0.4$ (note the temperature differences are scaled by a factor of 10 in the figure to make them visible). The temperature is more sensitive to differences in the model formulas than the density.

The parameter α_T accounts for factors not present in the harmonic cell model expressions. The expansion of the lattice is determined principally by the third derivative of the local potential energy surface [82]. An approximate treatment of the linear thermal expansion of a crystal [82] has a term $\sim \phi^{(3)}/r_1[\phi^{(2)}]^2 \sim n^{-1}$, where the derivatives are evaluated at $r = r_1$, and $\phi^{(k)}$ is the k th r -derivative of ϕ . This term has a magnitude of about 0.1 for $n = 12$ (the dominant term in the LJ potential), which is close to the optimum value of α_T found for the present analysis.

The present treatment of thermal expansion along the SL given in Eq. (21) has some features in common with that of van der Hoef [80] (see also Ref. [83]), however in that study the anharmonic effects were taken into account via a temperature-dependent polynomial correction term which was fitted to simulation SL data. The present treatment gives just as good a representation of the simulation SL data with only the single adjustable parameter, α_T . Note that Eq. (21) is based on the regular lattice summation formula for the pressure, whereas other studies have started typically from an approximate expression for the free energy, and taken its first density derivative to obtain the pressure [43,83,84].

Figure 10(b) presents in the same figure a comparison between the simulation-derived melting and sublimation lines with the simple approximated formulas given in Eqs. (4) and Eq. (22), respectively. The agreement is very good apart from close to the triple point for the ML, despite the fact that only the ML is an isomorph (not too close to the triple point), as is evident in Fig. 10(b). The sign difference between Eqs. (4) and Eq. (22) combined with different constants is sufficient to reflect this major qualitative difference in behavior.

Figure 11 shows the radial distribution function (RDF) at selected state points along the melting and sublimation lines, where the pair separation, r , is scaled by $\rho^{1/3}$. For the state points shown, the melting line is seen to be an isomorph, as the three curves are statistically the same (apart from near the tip of the first peak, the reason for which has been explained in Refs. [85,86]). In contrast, the RDFs along the sublimation line do not superimpose, indicating that the sublimation line is not an isomorph. This might be expected, as the melting line near the triple point departs from an isomorph [36]. Figure 11 demonstrates that the melting line RDF for $T = 3.5$ coincides well with those at higher density, whereas the δ_D^2 (see Fig. 6) and MF PDF for this temperature are still shifted from any higher density limiting values at this temperature, which is

TABLE II. Comparison of the sublimation densities from Refs. [17,18] denoted by ρ_{SK} , and ρ_{sub} from Eq. (21) with $\alpha_T = 0.11555$.

T	ρ_{SK}	ρ_{sub}	T	ρ_{SK}	ρ_{sub}
0.00	1.09151	1.09151	0.3	1.04512	1.04573
0.01	1.09010	1.09014	0.4	1.02722	1.02778
0.05	1.08437	1.08455	0.5	1.00755	1.00789
0.1	1.07702	1.07734	0.6	0.985365	0.985396
0.15	1.06944	1.06989	0.7	0.959192	0.959179

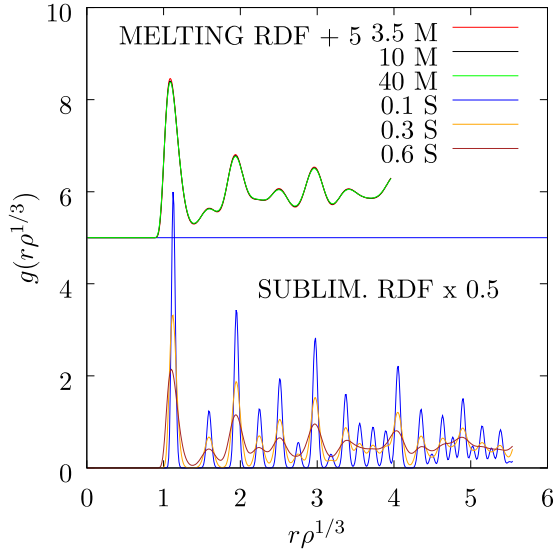


FIG. 11. Radial distribution functions along the melting and sublimation lines, for $N = 500$ and 1372 , respectively. The pair separation distance, r , is scaled by $\rho^{1/3}$. The values of T are given in the figure. The top three curves in the key are for the melting line (“M”), which are shifted vertically by 5, and the bottom three curves are for the sublimation line (“S”).

not achieved even for $T = 40$. Therefore, the convergence towards isomorphic scaling for fluctuation-based quantities is slower with increasing temperature (density) than the static average quantities such as the RDF, energy, and pressure. This conclusion is consistent with the linear relationship found in Fig. 8 as those state points are the ones that depart to some extent from an isomorph (i.e., where δ_D^2 is constant).

Figure 12 presents the density dependence of the force constant, K , along the sublimation line (via MD simulations carried out along the $P = 0$ line by the procedure explained in Sec. II B). The force constant was calculated by different routes using the formulas given in Sec. II A. Figure 12 should be compared with Fig. 5, which plots the same quantities for the melting line. Just as for melting, the SL K_p and K_T both increase in magnitude with increasing density (but for decreasing temperature in this case). They meet in the $T \rightarrow 0$ limit, whereas for melting they get farther apart with increasing ρ (note the log abscissa scale in Fig. 5). The perfect lattice force constant at each density, K_p , is again smaller than K_T . Numerical agreement between the two definitions of K_T in Eq. (11) was found, even at these very low temperatures. The force constant based on the MD data or K_D , which is defined in Eq. (12), exhibits a systematic decrease in magnitude with increasing system size, reflecting a progressive increase in the MSD with system size. There is not the same sensitivity to system size of K_D along the melting line.

Figure 13 shows δ^2 as a function of density along the sublimation line. The δ_p^2 and δ_T^2 were calculated from K_p and K_T using Eq. (13), and δ_D^2 was computed directly from the MD simulations using Eq. (12). Computations using METROPOLIS MC [57] were also carried out to establish if there are any artificial consequences of the lower than usual temperatures used in the SL simulations. The MC moves do not

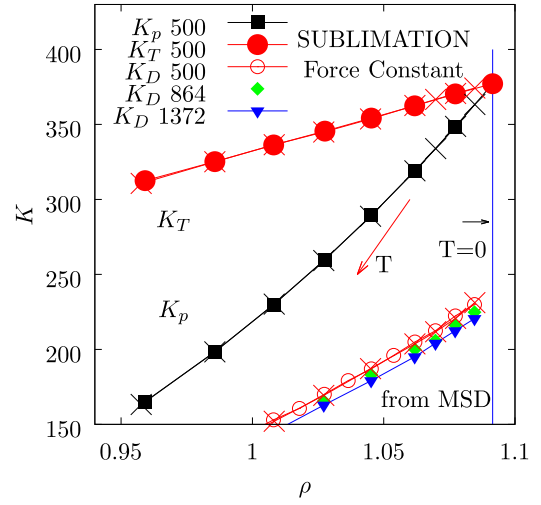


FIG. 12. The density dependence of the force constants along the LJ sublimation line. K_p is evaluated from Eq. (8) applied to a perfect lattice at the given density. K_T is defined in Eq. (11), and K_D is in Eq. (12). The T values are from right to left between 0.0, 0.1, 0.2, \dots , 0.7. The number of atoms used in the simulation is indicated in the figure. The crosses indicate the Nosé-Hoover thermostat ($N = 500$) while the other symbols are using the velocity scaling thermostat.

conserve the center of mass (even without periodic boundary crossings), which needs correcting in order to obtain physically meaningful MSD. For every N trial displacement, the average displacement per atom along each Cartesian

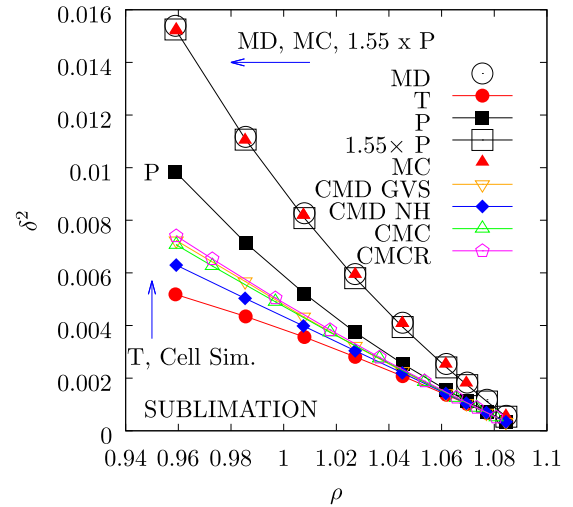


FIG. 13. As for Fig. 12, except the scaled mean-square displacements, δ^2 , along the sublimation line calculated by several procedures are shown, where “P” refers to δ_p^2 and “T” denotes δ_T^2 . The results for MD and Monte Carlo simulations (“MC”) are shown. The cell simulation variants on the figure are discussed in the main text. Note that temperature increases from right to left. The simulations were carried out with $N = 1372$ atoms.

direction was subtracted off, i.e.,

$$\begin{aligned}\bar{\delta\mathbf{r}} &= \frac{1}{N} \sum_{k=1}^N \delta\mathbf{r}_k, \\ \delta\mathbf{r}'_i &= \delta\mathbf{r}_i - \bar{\delta\mathbf{r}},\end{aligned}\quad (24)$$

where $\delta\mathbf{r}_k$ is the “displacement” (either $\mathbf{0}$ if the trial move is not accepted, or the accepted trial displacement) of particle k , and $\bar{\delta\mathbf{r}}$ is its average over N consecutive trial MC moves. The displacement for atom i used in computing the MSD is $\delta\mathbf{r}'_i$. This corrected displacement quantity is *only* used to compute the MSD, and the standard METROPOLIS MC procedure was used to evolve the particle positions without any center-of-mass corrections.

The MC simulation MSD values are statistically indistinguishable from the corresponding MD data, δ_D^2 , as may be seen in Fig. 13. The figure also shows data from the various cell simulation models, which agree quite well (apart from the NH CMD method) and are slightly above δ_T^2 to an extent that decreases with increasing ρ . There is a qualitative difference between δ_p^2 and δ_T^2 , being convex and concave, respectively, a trend that is not found for the melting line. As for the melting curve, the harmonic models significantly underestimate the MSD along the sublimation line. The figure reveals that a scaling factor of 1.55 applied to (this time) the δ_p^2 gives values that agree very well with those computed directly by MD or δ_D^2 using Eq. (12). The shape of δ_T^2 is concave, unlike for melting, and thus multiplication by a constant cannot make it agree with δ_D^2 (which is convex). Cooperative motion appears to be a significant factor for sublimation (just as for the ML) because of the significant difference between δ_T^2 and δ_D^2 . Figure 13 is another demonstration that the sublimation line is not an isomorph as δ_D^2 is not constant along it.

Figure 14(a) shows the repulsive (r^{-12}), attractive (r^{-6}) components and total potential energy per particle, u , along the $P = 0$ isobar. The HLR data for the regular static lattice at each density [see Eq. (5)] denoted by $u_{p,r}$, $u_{p,a}$, and u_p are presented in the figure. The corresponding MD data u_r , u_a , and u are also given. Figure 14(a) shows that within simulation statistics, the MD u values agree with the harmonic prediction for this quantity, $u_p + 3k_B T/2$, where $3k_B T/2$ is the vibrational contribution to the total potential energy in the classical harmonic approximation. The repulsive part of the potential energy decreases less rapidly than the static lattice value with increasing temperature (right to left in the figure). The differences between MD and the perfect lattice results are less pronounced for the attractive part of the potential energy.

Figure 14(b) presents the corresponding simulation and cell model quantities for the interaction components of the pressure. The repulsive and attractive components of the pressure from simulation and cell model to a large extent cancel each other out, which is expected as the total potential energy contribution to the pressure is hardly distinguishable from zero on that scale. In addition, the total interaction part of the pressure from the cell model is about an order of magnitude larger than from the MD simulations, but is still relatively small compared to the repulsive and attractive term components. The ratio of the MD divided by regular lattice

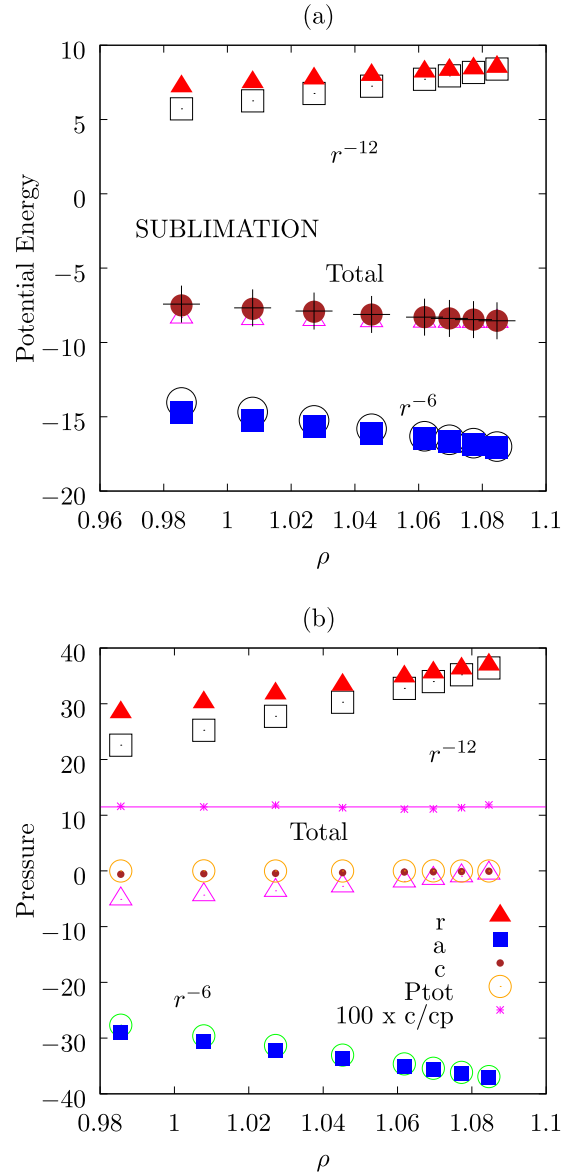


FIG. 14. (a) The components and total potential energy per particle, u , as a function of ρ along the $P = 0$ isobar of the LJ system, where $N = 1372$. The open symbols are for the perfect static lattice values, $u_{p,r}$, $u_{p,a}$, and u_p for repulsive, attractive, and total potential energy, respectively [see Eq. (7)]. The filled-in symbols denote the simulation averages at each density (temperature). The crosses are $u_p + 3k_B T/2$. Frame (b) is the corresponding plot for the interaction components of the pressure. The open orange circles are for the total pressure (“ P_{tot} ”) of the system obtained directly by MD, which includes both kinetic and potential energy terms. Also, $c_p = u_{p,r} + u_{p,a}$ and $c = u_r + u_a$. The magenta * are the ratio of the MD and regular lattice total interaction parts of the pressure, c/c_p , which correspond to the variable, α_T , in Eq. (21).

predictions of the interaction part of the pressure in Fig. 14 is independent of density to a good approximation, and equals α_T .

Figure 15 presents the melting factor plots for the sublimation line, in the same format as for the melting line shown in Fig. 8. The MF trends in both frames (a) and (b) are the same

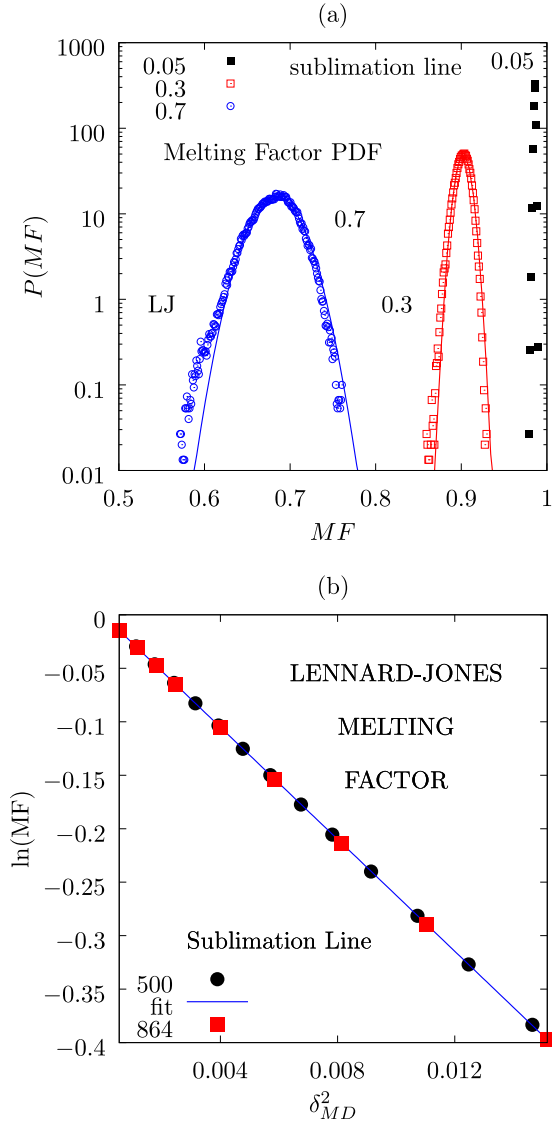


FIG. 15. (a) Melting factor PDF for the sublimation line at three temperatures, $T = 0.05$, 0.3 , and 0.7 . MD data for $N = 500$ are shown. (b) The mean melting factor against δ_D^2 [see Eq. (19)].

for melting and sublimation when plotted against the MD determined values of δ . Notably in Fig. 15(a) as temperature increases there develops a shoulder in the MF PDF which is indicative of occasional large disruptive displacements of the atoms through cooperative motion. The slope of $-26.19(2)$ in Fig. 15(b) is close to the exact limit of -26.32 given in Eq. (19), which is even better than the value obtained for the ML.

IV. CONCLUSIONS

This study has shown that the sublimation line of the Lennard-Jones system is not an isomorph and is not predicted even qualitatively correctly by harmonic cell models. This is in contrast to the melting line, which is a very good isomorph except close to the triple point. Despite this difference, the atom mean-square displacements of the two lines generated by molecular dynamics simulations can be reproduced by the

harmonic cell models on the application of scaling factors to include the effects of anharmonicity and cooperative motion at a mean-field level, as was first shown by Holian [23] for the melting line. The extent of agreement is shown here to improve considerably if molecular-dynamics simulations are used to compute a time average effective lattice harmonic force constant employed in the cell model. Lattice caged single-atom molecular dynamics and Monte Carlo simulations were also carried out on isolated atoms to concentrate on the effects of anharmonicity by eliminating the collective motion. The probability distribution function of the melting factor showed that large displacement event departures from harmonic motion and Gaussian statistics do occur (evident in the lower wing of the PDF). The melting factor as a function of the mean-square displacement (normalized by the nearest-neighbor distance) is accurately represented by the Debye-Waller factor for both the melting and sublimation lines.

It was found here that the sublimation line can be represented accurately by the simple analytic expression $k_B T = a\rho^4 + b\rho^2$, where the a and b constants are negative and positive, respectively, which is a new result. This relationship has been found previously for the melting line, but the two constants are positive and negative, respectively, in that case. For the sublimation line, this formula can be derived starting from a static perfect lattice expression for the pressure and assuming the total pressure is zero [see Eq. (21)], which is an accurate approximation, and then making a semiempirical generalization. The interaction part of the total pressure of the crystal is negative along the sublimation boundary line.

It is proved that the harmonic cell model prediction for the melting line can be physically unrealistic for purely repulsive potential systems under certain conditions, as the dimensionless route mean-square displacement parameter exceeds unity. This is the case for inverse power solids with exponent, n , greater than about 40, and for the WCA system for reduced temperatures below about 0.01. *Inter alia* the analysis carried out here for the WCA solid boundary produces a simple accurate analytic expression for the melting line of the WCA system in the low-temperature regime using a hard-sphere reference, which is a valid approximation at these very low temperatures [see Eq. (16)].

A formal relationship between melting indicator and harmonic cell models is derived, and their predictions along the melting line are shown to be qualitatively the same. The near constancy of their characteristic parameters along the melting line is consistent with the predictions of isomorph theory and an approximate isomorph [79].

To conclude, the results and analysis of this work indicate that there are previously unrecognized connections in the density-temperature dependence of the Lennard-Jones melting and sublimation lines despite the fact that they have opposite slopes. The mean-square displacements for both lines can be predicted well by harmonic cell models with mean-field corrections for anharmonicity effects and collective motion. We think that it would be interesting to attempt to explain at a more fundamental (statistical mechanical) level why the melting and sublimation lines of the LJ solid can *both* be represented by a simple formula, especially as the sublimation line is not an isomorph whereas the melting line

is one to a good approximation. Further investigation could be carried out to determine if the same trends are evident for systems in which the atoms interact with other potentials such as the more general $n : m$ or Mie potential defined in Eq. (1), possibly using the lattice constants in Table I. It should be noted, however, that the coexistence lines for other examples of the $n : m$ potential are less well established from simulation compared to the Lennard-Jones special case, which would make this a fairly demanding computational project. Such analyses might provide a foundation for a more rigorous “unified” statistical mechanical description of these two solid-fluid boundaries.

ACKNOWLEDGMENT

D.M.H. would like to thank Dr. T. Crane (Department of Physics, Royal Holloway, University of London, UK) for helpful software support.

APPENDIX A: RADIAL DISPLACEMENT DENSITY DISTRIBUTION

Details are given of the radial density distribution, $\rho(\Delta\mathbf{r})$, as a function of the departure of an atom from its mean lattice site, $\Delta\mathbf{r}$. Models for solids frequently represent the density profile of the atom around its mean coordinate, $\rho(\Delta\mathbf{r})$, by a Gaussian centered on the lattice site [75],

$$\begin{aligned}\rho(\Delta\mathbf{r}) &= \left(\frac{\alpha_G}{\pi}\right)^{3/2} e^{-\alpha_G[\Delta\mathbf{r}]^2}, \\ \langle[\Delta\mathbf{r}]^2\rangle &= 4\pi\left(\frac{\alpha_G}{\pi}\right)^{3/2} \int_0^\infty x^4 e^{-\alpha_G x^2} dx \\ &= \frac{3}{2\alpha_G} = \delta^2 r_1^2.\end{aligned}\quad (\text{A1})$$

Without making any assumptions about the analytic form of $\rho(\Delta\mathbf{r})$, it is convenient to define a radial probability

distribution function, $P(\Delta r)$,

$$\begin{aligned}P(\Delta r) &= \frac{\int d\Omega \rho(\Delta\mathbf{r})[\Delta r]^2 d\Delta r}{\int d\Omega \rho(\Delta\mathbf{r}) \int [\Delta r]^2 d\Delta r} \simeq \frac{\Delta N(\Delta r \pm \frac{\delta\Delta r}{2})}{\sum \Delta N}, \\ \rho(\Delta r) &= \frac{P(\Delta r)}{4\pi[\Delta r]^2 d\Delta r} \simeq \frac{\Delta N(\Delta r \pm \frac{\delta\Delta r}{2})}{\Delta V(\Delta r) \sum \Delta N}, \\ \Delta V(\Delta r) &\simeq \frac{4}{3}\pi \left[\left(\Delta r + \frac{\delta\Delta r}{2}\right)^3 - \left(\Delta r - \frac{\delta\Delta r}{2}\right)^3 \right].\end{aligned}\quad (\text{A2})$$

The integral in the first line of Eq. (A2) is over the solid angle, Ω . The number of occurrences of the atom at $\Delta\rho(r)$ which is within the shell, $\Delta r \pm \delta\Delta r/2$, is denoted by $\Delta N(\Delta r \pm \delta\Delta r/2)$, and $\Delta V(\Delta r)$ is the volume element of that shell. The formulas involving ΔN in Eq. (A2) are in a form convenient for numerical evaluation within an MD program.

APPENDIX B: THE MELTING INDICATOR

The melting indicator parameter, \mathcal{L} , introduced in Eq. (20) for the Mie potential is

$$\mathcal{L} = \frac{Q}{k_B T} \left(\frac{n(n+1)}{c^n} \rho^{n/3} - \frac{m(m+1)}{c^m} \rho^{m/3} \right). \quad (\text{B1})$$

Equation (B1) is a generalization of the formula given in Refs. [37,53]. The HLR formula in Eq. (9) can be reexpressed to bring out its relationship to Eq. (B1). If the quantity $B'_k = B_k/[Qk(k-1)N_1]$ is defined, then

$$\begin{aligned}\mathcal{M} &\equiv \frac{9}{\delta^2 N_1} \\ &= \frac{Q}{k_B T} \left(\frac{n(n-1)}{c^n} B'_n \rho^{n/3} - \frac{m(m-1)}{c^m} B'_m \rho^{m/3} \right).\end{aligned}\quad (\text{B2})$$

For the LJ system along the ML, the $T_s(\rho_s)$ is known accurately [17,18], which is employed in Eqs. (B1) and (B2). The values of B'_{12} and B'_6 for the sc and fcc lattices are given in the caption to Fig. 9, which shows the density dependence of \mathcal{L} and \mathcal{M} along the ML using the sc lattice and the fcc lattice.

-
- [1] W. G. Hoover and M. Ross, *Contemp. Phys.* **12**, 339 (1971).
 - [2] R. Agrawal and D. A. Kofke, *Phys. Rev. Lett.* **74**, 122 (1995).
 - [3] U. R. Pedersen, *J. Chem. Phys.* **139**, 104102 (2013).
 - [4] A. B. Belonoshko, N. V. Skorodumova, A. Rosengren, and B. Johansson, *Phys. Rev. B* **73**, 012201 (2006).
 - [5] B. J. Alder and T. E. Wainwright, *J. Chem. Phys.* **33**, 1439 (1960).
 - [6] M. Ross, *Phys. Rev.* **184**, 233 (1969).
 - [7] F. Saija, S. Prestipino, and P. V. Giaquinta, *J. Chem. Phys.* **124**, 244504 (2006).
 - [8] S. Pieprzyk, D. M. Heyes and A. C. Brańka, *Phys. Rev. E* **90**, 012106 (2014).
 - [9] J. E. Lennard-Jones and A. F. Devonshire, *Proc. Roy. Soc. (London) A* **163**, 53 (1937).
 - [10] J. A. Barker, *Lattice Theories of the Liquid State* (Macmillan, New York, 1963).
 - [11] J. A. Barker, *Proc. R. Soc. A* **230**, 390 (1955).
 - [12] W. G. Hoover and F. H. Ree, *J. Chem. Phys.* **47**, 4873 (1967).
 - [13] W. G. Hoover and W. T. Ashurst, *J. Chem. Phys.* **57**, 1259 (1972).
 - [14] R. J. Henchman, *J. Chem. Phys.* **126**, 064504 (2007).
 - [15] A. Chakravorty, J. Higham, and R. H. Henchman, *J. Chem. Inf. Model.* **60**, 5540 (2020).
 - [16] B. M. Mladek, P. Charbonneau, C. N. Likos, D. Frenkel, and G. Kahl, *J. Phys.: Condens. Matter* **20**, 494245 (2008).
 - [17] A. J. Schultz and D. A. Kofke, *J. Chem. Phys.* **149**, 204508 (2018).
 - [18] A. J. Schultz and D. A. Kofke, *J. Chem. Phys.* **153**, 059901 (2020).
 - [19] A. N. Singh, J. C. Dyre, and U. R. Pedersen, *J. Chem. Phys.* **154**, 134501 (2021).
 - [20] F. H. Stillinger, *J. Chem. Phys.* **65**, 3968 (1976).
 - [21] C. N. Likos, *Phys. Rep.* **348**, 26 (2001).
 - [22] W. G. Hoover, M. Ross, K. W. Johnson, D. Henderson, J. A. Barker, and B. C. Brown, *J. Chem. Phys.* **52**, 4931 (1970).
 - [23] B. L. Holian, *Phys. Rev. B* **22**, 1394 (1980).

- [24] C. Bhattacharya, M. K. Srivastava, and S. V. G. Menon, *Phys. B: Condens. Matter* **406**, 4035 (2011).
- [25] J. D. Weeks, D. Chandler, and H. C. Andersen, *J. Chem. Phys.* **54**, 5237 (1971).
- [26] R. J. Sadus, *J. Chem. Phys.* **149**, 074504 (2018).
- [27] S. S. Xantheas and J. C. Werhahn, *J. Chem. Phys.* **141**, 064117 (2014).
- [28] G. Rickayzen and D. M. Heyes, *J. Phys.: Condens. Matter* **19**, 416101 (2007).
- [29] R. Agrawal and D. A. Kofke, *Mol. Phys.* **85**, 23 (1995).
- [30] G. C. McNeil-Watson and N. B. Wilding, *J. Chem. Phys.* **124**, 064504 (2006).
- [31] J. M. G. Sousa, A. L. Ferreira, and M. A. Barroso, *J. Chem. Phys.* **136**, 174502 (2012).
- [32] W. G. Hoover, S. G. Gray, and K. W. Johnson, *J. Chem. Phys.* **55**, 1128 (1971).
- [33] E. A. Mastny and J. J. de Pablo, *J. Chem. Phys.* **127**, 104504 (2007).
- [34] A. Ahmed and R. J. Sadus, *J. Chem. Phys.* **133**, 124515 (2010).
- [35] D. M. Heyes and A. C. Brańka, *J. Chem. Phys.* **143**, 234504 (2015).
- [36] U. R. Pedersen, L. Costigliola, N. P. Bailey, T. B. Schröder and J. C. Dyre, *Nat. Commun.* **7**, 12386 (2016).
- [37] S. A. Khrapak, M. Chaudhuri, and G. E. Morfill, *Phys. Rev. B* **82**, 052101 (2010).
- [38] S. A. Khrapak and G. E. Morfill, *J. Chem. Phys.* **134**, 094108 (2011).
- [39] L. Separdar, N. P. Bailey, T. B. Schröder, S. Davatolhagh and J. Dyre, *J. Chem. Phys.* **138**, 154505 (2013).
- [40] L. Bøhling, T. S. Ingebrigtsen, A. Grzybowski, P. Paluch, J. C. Dyre, and T. B. Schröder, *New J. Phys.* **14**, 113035 (2012).
- [41] Y. Rosenfeld, *J. Chem. Phys.* **63**, 2769 (1974).
- [42] Y. Rosenfeld, J. E. Avron, S. Goshen, and R. Thieberger, *J. Chem. Phys.* **66**, 2758 (1977).
- [43] Y. Rosenfeld, *Mol. Phys.* **32**, 963 (1976).
- [44] R. K. Crawford, *J. Chem. Phys.* **60**, 2169 (1974).
- [45] G. Rastelli and E. Cappelluti, *Phys. Rev. B* **84**, 184305 (2011).
- [46] S. A. Khrapak and F. Saija, *Mol. Phys.* **109**, 2417 (2011).
- [47] S.-N. Luo, A. Strachan, and D. C. Swift, *J. Chem. Phys.* **122**, 194709 (2005).
- [48] I. Nikiteas and D. M. Heyes, *Phys. Rev. E* **102**, 042102 (2020).
- [49] F. H. Stillinger, *J. Chem. Phys.* **115**, 5208 (2001).
- [50] U. Balucani and M. Zoppi, *Dynamics of the Liquid State* (Clarendon, Oxford, 1994), p. 290.
- [51] J. G. Powles, G. Rickayzen, and D. M. Heyes, *Mol. Phys.* **103**, 1361 (2005).
- [52] S. A. Khrapak and G. E. Morfill, *Phys. Rev. Lett.* **103**, 255003 (2009).
- [53] S. A. Khrapak, M. Chaudhuri, and G. E. Morfill, *J. Chem. Phys.* **134**, 054120 (2011).
- [54] L. Costigliola, T. B. Schröder, and J. C. Dyre, *Phys. Chem. Chem. Phys.* **18**, 14678 (2016).
- [55] D. M. Heyes, *The Liquid State: Applications of Molecular Simulations* (Wiley, Chichester, 1998).
- [56] W. G. Hoover, *Phys. Rev. A* **31**, 1695 (1985).
- [57] M. P. Allen and D. J. Tildesley, *Computer Simulation of Liquids* (Oxford University Press, Oxford, 2017).
- [58] See Supplemental Material at <http://link.aps.org/supplemental/10.1103/PhysRevE.104.044119> for further figures relating to the melting line, and tables of the lattice summation constants relating to Tables I and II for the different potentials and crystal lattice classes considered in this study.
- [59] A. Ahmed and R. J. Sadus, *J. Chem. Phys.* **131**, 174504 (2009).
- [60] A. Ahmed and R. J. Sadus, *Phys. Rev. E* **80**, 061101 (2009).
- [61] A. Ahmed and R. J. Sadus, *Phys. Rev. E* **99**, 029901(E) (2019).
- [62] A. de Kuiper, J. A. Schouten, and J. P. J. Michels, *J. Chem. Phys.* **93**, 3515 (1990).
- [63] S. Pieprzyk, M. N. Bannerman, A. C. Brańka, M. Chudak and D. M. Heyes, *Phys. Chem. Chem. Phys.* **21**, 688 (2019).
- [64] A. D. Booth, *J. Comput. Phys.* **46**, 423 (1982).
- [65] G. A. Wolfe and B. Goodman, *Phys. Rev.* **178**, 1171 (1969).
- [66] A. R. Ruffa, *Phys. Rev. B* **24**, 6915 (1981).
- [67] R. C. Shukla and C. A. Plint, *Phys. Rev. B* **40**, 10337 (1989).
- [68] A. A. Maradudin, P. A. Flinn, and R. A. Coldwell-Horsfall, *Ann. Phys.* **15**, 337 (1961).
- [69] A. A. Maradudin, P. A. Flinn, and R. A. Coldwell-Horsfall, *Ann. Phys.* **15**, 360 (1961).
- [70] P. A. Flinn and A. A. Maradudin, *Ann. Phys.* **22**, 223 (1963).
- [71] A. A. Maradudin and P. A. Flinn, *Phys. Rev.* **129**, 2529 (1963).
- [72] F. W. de Wette, L. H. Fowler, and B. R. A. Nijboer, *Physica* **54**, 292 (1971).
- [73] U. Buchenau, R. Zorn, and M. A. Ramos, *Phys. Rev. E* **90**, 042312 (2014).
- [74] S. A. Khrapak, *Phys. Rev. Research* **2**, 012040(R) (2020).
- [75] C. N. Likos, B. M. Mladek, A. J. Moreno, D. Gottwald, and G. Kahl, *Comput. Phys. Commun.* **179**, 71 (2008).
- [76] J. P. Hansen and L. Verlet, *Phys. Rev.* **184**, 151 (1969).
- [77] S. R. Phillpot, S. Yip, and D. Wolf, *Comput. Phys.* **3**, 20 (1989).
- [78] D. M. Heyes and A. C. Brańka, *Phys. Status Solidi B* **252**, 1514 (2015).
- [79] L. Bøhling, N. P. Bailey, T. B. Schröder, and J. C. Dyre, *J. Chem. Phys.* **140**, 124510 (2014).
- [80] M. A. van der Hoef, *J. Chem. Phys.* **117**, 5092 (2002).
- [81] C. Calero, C. Knorowski, and A. Travesset, *J. Chem. Phys.* **144**, 124102 (2016).
- [82] T. Ishiti, S. Naya, and S. Tanaka, *Prog. Theor. Phys.* **69**, 1074 (1983).
- [83] M. A. van der Hoef, *J. Chem. Phys.* **113**, 8142 (2000).
- [84] Y. Rosenfeld and J. E. Avron, *J. Chem. Phys.* **64**, 1248 (1976).
- [85] L. Bøhling, A. A. Veldhorst, T. S. Ingebrigtsen, N. P. Bailey, J. S. Hansen, S. Toxvaerd, T. B. Schröder, and J. C. Dyre, *J. Phys.: Condens. Matter* **25**, 032101 (2013).
- [86] S. Toxvaerd and J. C. Dyre, *J. Chem. Phys.* **135**, 134501 (2011).